Supplement of The Cryosphere, 12, 1499–1510, 2018
https://doi.org/10.5194/tc-12-1499-2018-supplement

Supplement of

The influence of atmospheric grid resolution in a climate model-forced ice sheet simulation

Marcus Lofverstrom and Johan Liakka

Correspondence to: Marcus Lofverstrom (marcusl@ucar.edu)

S1 Topography

Figure S1 compares the resolved LGM topography on the different horizontal resolutions. The full fields are shown in the left columns (panels a-d), and differences with respect to the T85 case are shown on the right (panels e-g). The spurious positive and negative anomalies seen over the ocean in the difference plots (panels e-g) are so called Gibbs oscillations from the spherical harmonic transforms. In short, all linear operations in the dynamical core (e.g. calculation of spatial gradients) are carried out in spectral space, whereby the fields are projected onto truncated series of spherical harmonics (orthogonal eigenfunctions of the Laplace equation on a sphere). When transforming the fields back to grid-space, spurious oscillations tend to occur in regions with sharp transitions/changes (e.g. on the ice sheet edges and the land-ocean boundaries) as these are hard to represent by a truncated series of trigonometric functions.

The resolved topography is largely comparable in the T42 and T31 cases, but it is substantially different on the T21 grid. While the interior of the Laurentide Ice Sheet retains much of its height (difference in the interior is of order 200 m in the T21 case), the ice-sheet edges suffer from substantial height loss. Similarly, the Eurasian Ice Sheet – which is relatively narrow and therefore not well captured by only 21 harmonics – is 500 to 1000 m lower than the T85 case (Fig. S1g).

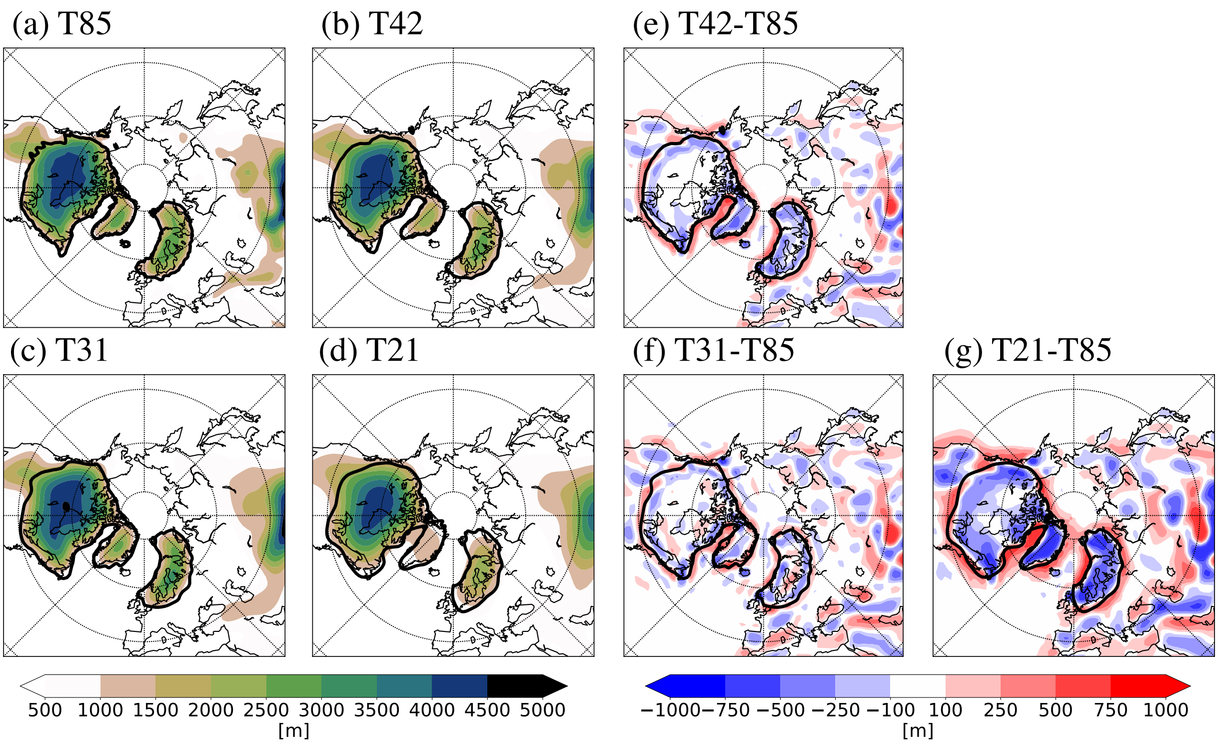

Figure S1: Resolved LGM topography [m] on the different horizontal grids. The full fields are shown in the left panels (a–d), and the difference with respect to the T85 case is shown on the right (e–g). The 500 m ice sheet topography from the LGM reconstruction is indicated by the heavy contours (interpolated to the different horizontal resolutions).

S2 Atmospheric lapse rate

Figure S2 shows the JJA surface temperature difference when extrapolating the LGM temperatures to the modern day topography (temperature used by the ice sheet model upon initialization). The left panels (a-d) use the modern global temperature lapse rate of 6.5 °C km^{-1} (same as in main paper), and the right panels (e-h) a lapse rate of 4.6 °C km^{-1}, which is based on modern observations over the Greenland ice sheet (Fausto et al., 2009). Although some of the positive temperature anomalies seen in the left panels are suppressed when using the lower lapse rate, it is hard to motivate this choice because of the glacial context of the study. It is not obvious that modern day observations over the Greenland ice sheet are suitable for the conditions over mid- and high-latitude ice sheets at the last glacial maximum (this climate was considerably colder and therefore drier than present; Braconnot et al., 2007). Modeling experiments have also shown that the influence of the lapse rate can be offset by varying other (largely unconstrained) parameter values. For example Stone et al. (2010) simulated a reasonable modern Greenland geometry with atmospheric lapse rates as different as 4 and 8 °C km^{-1}, by instead using the PDD factors to tune the surface mass balance.

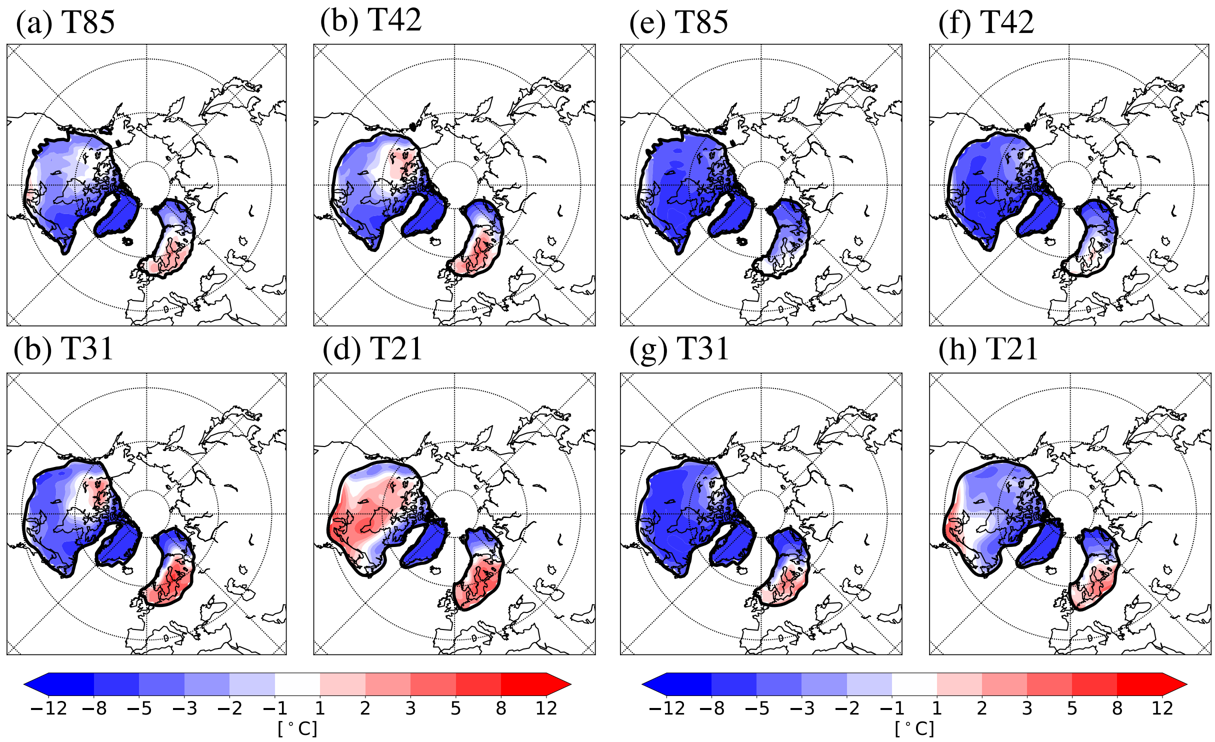

Figure S2: JJA surface temperature [°C] over the LGM ice sheet when extrapolated to the height of the modern topography (temperature seen by ice-sheet model upon initialization). The left columns (a-d) use the standard atmospheric lapse rate of 6.5 °C km^{-1}, and the right columns the "observed" July lapse rate (4.6 °C km^{-1}) over the Greenland ice sheet (Fausto et al., 2009). The 500 m ice-sheet height from the LGM reconstruction is indicated by the heavy contours (interpolated to the different horizontal resolutions)

S3 Heat flux convergence by stationary waves

Figure S3 shows the nominal 850 hPa heat flux convergence by stationary waves ($-\partial_y \bar{v}^* \bar{T}^*$), where v and T denote meridional wind and temperature, overbar indicates time mean, and asterisk the deviation from zonal mean. The full fields are shown in the left columns (a-d), and the differences with respect to the T85 case are shown on the right (e-g). The weakening of the stationary waves in the T21 case (Fig. 1 in main text) results in a damped "cold air advection" over the Laurentide ice sheet, and thus a reduced cooling effect over the southern/southeastern parts of the ice sheet. The heat flux convergence by transient waves is about an order of magnitude smaller and therefore of second order importance for the narrative of the paper (not shown).

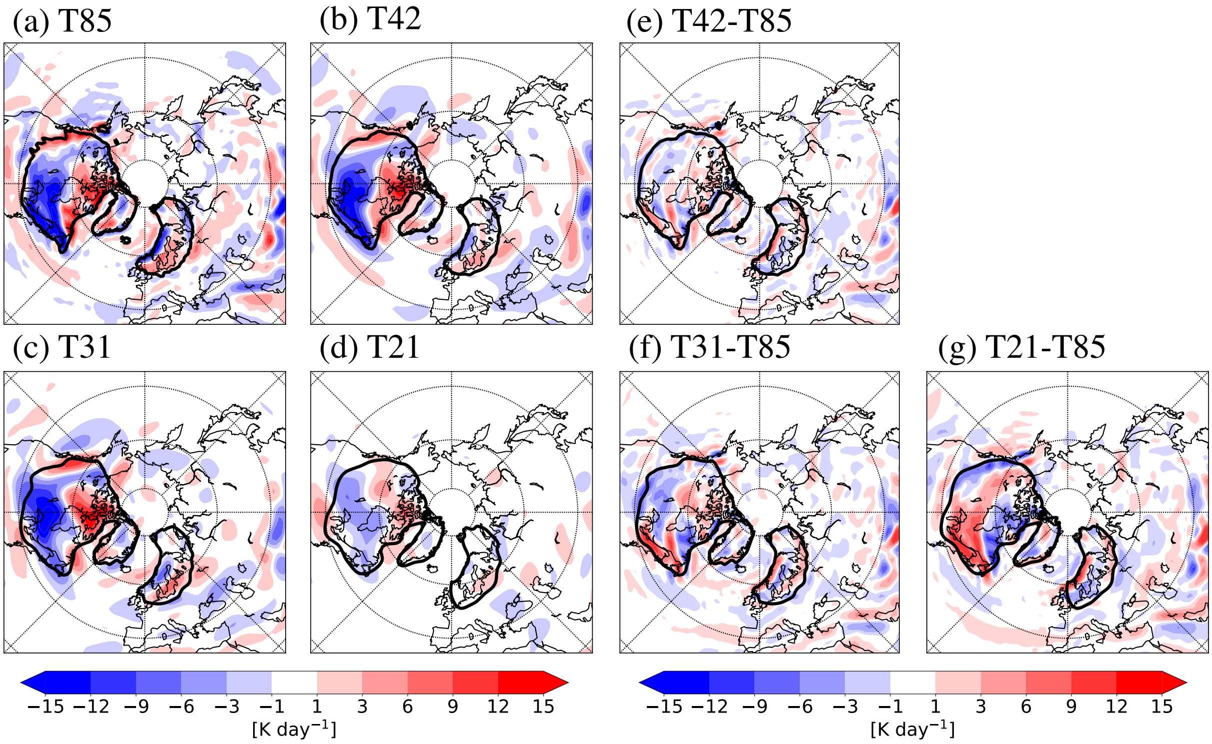

Figure S3: JJA heat flux convergence by stationary wave [K day^{-1}] on the nominal 850 hPa surface. The full fields are shown in the left panels (a–d), and the difference with respect to the T85 case is shown on the right (e–g). The 500 m ice sheet topography from the LGM reconstruction is indicated by the heavy contours (interpolated to the different horizontal resolutions).

S4 Surface radiative heating

Figure S4 shows the surface radiative heating ($SW_{net} + LW_{down}$). This term is used by the atmosphere model to calculate the surface temperature (Fig. 2 in main text). There is substantially more downwelling longwave radiation in response to the increased cloudiness (Fig. 1 in main text). The changes are of order 5 to 10 W m^{-2} in the T42 and T31 cases, but in excess of 30 W m^{-2} in the T21 case. This is thought to be the main reason for the surface warming (Fig. 2 in main text), together with the lapse-rate effect due to changes in the resolved topography (Fig. S1).

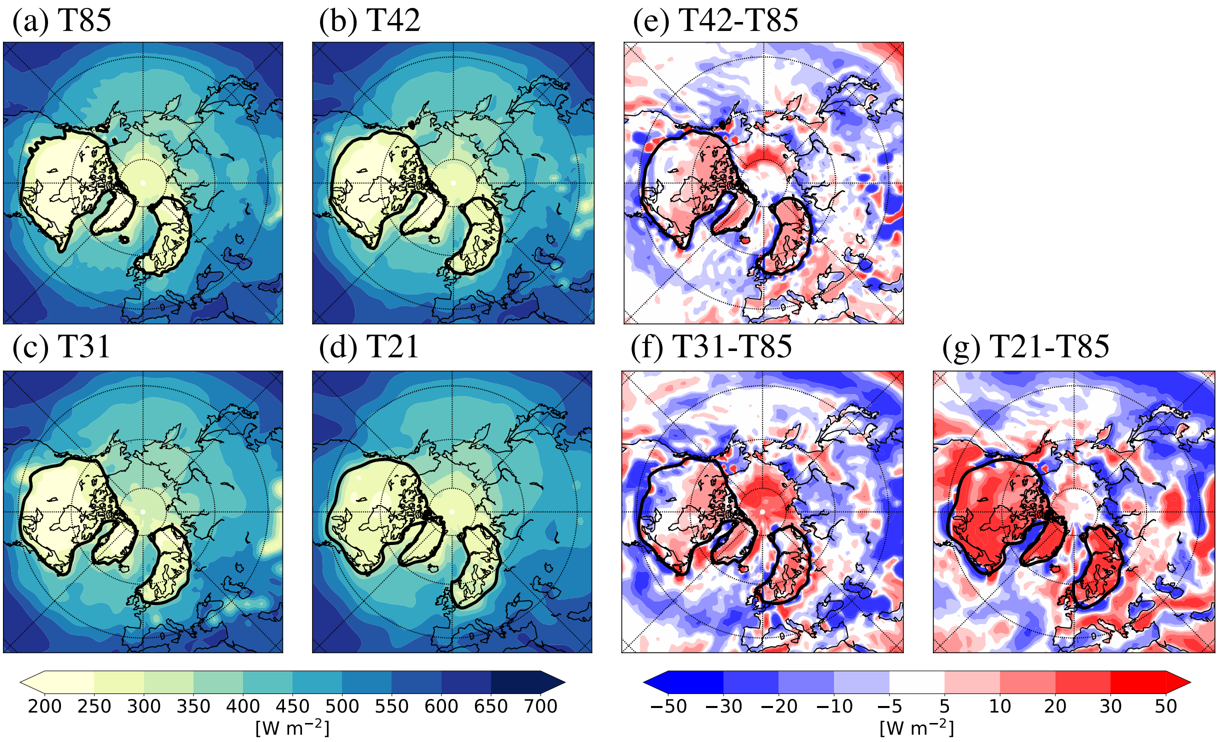

Figure S4: JJA surface radiative heating ($SW_{net} + LW_{down}$). The full fields are shown in the left panels (a–d), and the difference with respect to the T85 case is shown on the right (e–g). The 500 m ice sheet topography from the LGM reconstruction is indicated by the heavy contours (interpolated to the different horizontal resolutions).

References

Braconnot, P., Otto-Bliesner, B., Harrison, S., Joussaume, S., Peterchmitt, J.-Y., Abe-Ouchi, A., Crucifix, M., Driesschaert, E., Fichefet, T., Hewitt, C., Kageyama, M., Kitoh, A., Laine, A., Loutre, M.-F., Marti, O., Merkel, U., Ramstein, G., Valdes, P., Weber, S. L., Y, Y., and Y, Z.: Results of PMIP2 coupled simulations of the Mid-Holocene and Last Glacial Maximum–Part 1: experiments and large-scale features, Climate Past, 3, 261–277, 2007.

Fausto, R. S., Ahlstrom, A. P., Van As, D., Boggild, C. E., and Johnsen, S. J.: A new present-day temperature parameterization for Greenland, Journal of Glaciology, 55, 95–105, 2009.

Stone, E., Lunt, D., Rutt, I., and Hanna, E.: Investigating the sensitivity of numerical model simulations of the modern state of the Greenland ice-sheet and its future response to climate change, The Cryosphere, 4, 397–417, 2010.